AFM mapping of the elastic properties of brain tissue reveals kPa μm–1 gradients of rigidity

Nicolas Bouchonville, Mikaël Meyer, Christophe Gaude, Emmanuel Gay, David Ratel, Alice Nicolas

AFM mapping of the elastic properties of brain tissue reveals kPa μm^{-1} gradients of rigidity

Nicolas Bouchonville,[abc] Mikae¨l Meyer,[ad] Christophe Gaude,[ace] Emmanuel Gay,[ad] David Ratel[ace] and Alice Nicolas‡*[abc]

It is now well established that the mechanical environment of the cells in tissues deeply impacts cellular fate, including life cycle, differentiation and tumor progression. Designs of biomaterials already include the control of mechanical parameters, and in general, their main focus is to control the rheological properties of the biomaterials at a macroscopic scale. However, recent studies have demonstrated that cells can stress their environment below the micron scale, and therefore could possibly respond to the rheological properties of their environment at this micron scale. In this context, probing the mechanical properties of physiological cellular environments at subcellular scales is becoming critical. To this aim, we performed in vitro indentation measurements using AFM on sliced human pituitary gland tissues. A robust methodology was implemented using elasto-adhesive models, which shows that accounting for the adhesion of the probe on the tissue is critical for the reliability of the measurement. In addition to quantifying for the first time the rigidity of normal pituitary gland tissue, with a geometric mean of 9.5 kPa, our measurements demonstrated that the mechanical properties of this tissue are far from uniform at subcellular scales. Gradients of rigidity as large as 12 kPa μm^{-1} were observed. This observation suggests that physiological rigidity can be highly non-uniform at the micron-scale.

1 Introduction

Organs and biological tissues are soft, with rigidity spanning from less than 100 Pa within adipose tissues, to GPa in bones.[1] These values are averaged compliances of the entire organs, obtained by *ex vivo* macroscopic rheological measurements, for instance through rheometers,[2,3] stretching devices[4] or compressive devices[3,5] (see ref. 1 for a more detailed review). More resolved mechanical characterization is provided by magnetic resonance elastography (MRE)[6] and ultrasound elastography,[7] which allow an *in vivo*, non-destructive mapping of the rheological properties of tissues, from cm^3 down to mm^3. *In vivo* indentation could also reach these specifications on soft or hard tissues.[8,9] Going still down scale appears more and more relevant, as tissue cells were shown to orient their fate in accordance with the cell-scaled mechanical environment.[10–12] This issue recently came to the front stage as cells were proved to probe the rigidity of the extracellular matrix below the micron scale, by the contraction of their adhesion complexes.[13] And indeed, supramolecular force sensors were identified within the adhesion complexes named focal adhesions.[14–16]

Consequently, an issue is now quantification of the rigidity and the rigidity gradients cells are facing in a tissue at the micron scale. So far, only millimeter-scaled gradients of rigidity have been considered, and for instance their role in the development of the central nervous system has been emphasized.[17] But regarding the recent finding that cells could in principle probe micron-scaled rigidity,[15,16] elucidating micron-scaled rigidity in physiological tissues is to be performed. For this purpose, we propose here the first micron-scaled averaged mapping by IT-AFM of a brain tissue, the pituitary gland tissue. Micron scaled averaging is performed using a spherical AFM probe of 10 μm diameter. At the centimeter scale, the rheological behavior of brain tissues was shown to be visco-elastic with nonlinear properties and plasticity.[8,18,19] In the present article, we propose a methodology to address rigidity measurements by indentation first by setting up an easy handling criterion to mark out the linear elastic response to indentation. Second, we demonstrate that adhesive interactions between the probe and the tissue critically influence the quantification of the elastic modulus, and must be accounted. As our measurement shows here, the pituitary gland tissue is of intermediate

[a] University of Grenoble Alpes, Grenoble, France
[b] Centre National de la Recherche Scientifique, Laboratory of Technologies of Microelectronics, Grenoble, France
[c] CEA-Léti-Minatec, F38000, Grenoble, France
[d] Department of Neurosurgery, CHU de Grenoble – Hôpital Albert Michallon, Grenoble, France
[e] CEA-L´eti-Clinatec, F38000, Grenoble, France
‡ Current address: LTM c/o CEA-Le´ti, 17 rue des Martyrs, 38054 Grenoble cedex 9, France. E-mail: alice.nicolas@cnrs.fr; Fax: +33 438785892; Tel: +33 438789404.

stiffness compared to other organs.[1] Technical difficulties that are met here due to the use of a large probe and the potentially complex rheological behavior of the tissue are representative of many other tissues. The proposed methodology goes therefore beyond the measurement of this specific tissue and addresses indentation measurements on sticky elastic samples with a spherical probe.

2 Marking out the boundaries of the elastic regime

A critical issue in the determination of mechanical properties by indentation is the way data are fitted. Indeed, post-treatment dramatically influences the results depending on the part of the indentation curve that is fitted, because most of the samples are heterogeneous and/or exhibit non-linear properties.[20] Then it is worth setting up a methodology to determine what part of the indentation curve corresponds to the actual elastic response of the sample. Different fitting boundaries can result in a two times difference in the measured stiffness (see ESI,† Fig. S1). Fitting the right portion of the experimental curve is a long standing issue, which was presently solved by using a sliding or growing window strategy.[21,22] This technique involves a fit of the indentation data at multiple indentation depths and/or on a growing area of the curve. In general, the Young's modulus reaches a plateau which corresponds to the actual Young's modulus of the sample. This method proved very efficient for samples with simple behavior, such as thick polyacrylamide hydrogels, but is difficult to interpret in the case of thin[21] or multilayered samples (see ESI†). In addition, it is time consuming, because each indentation curve has to be fitted multiple times in order to reach the required accuracy that allows challenging the appropriateness of the model. Consequently, we adapted a method proposed by Cappella *et al.*[23] for pyramidal tips and non-adhesive materials to our case of spherical indenter and adhesive interaction between the probe and the tissue. This method consists in plotting the variation of the indentation force to the appropriate power law with the indentation depth. Thus, when assuming a purely elastic interaction between a spherical probe and the sample, this power law is 2/3 as predicted by Hertz's model:

$$F_n = K\delta^{3/2}R^{1/2} \quad (1)$$

with F_n being the normal, indenting force, δ the indentation depth, R the radius of curvature of the indenter and K the renormalized elastic modulus, related to the Young's modulus E and Poisson ratio ν by $K = 4/3E/(1 - \nu^2)$. Below we show that accounting for an additional adhesive interaction between the tip and the sample does not modify this exponent to zeroth order.

Theories have been developed to account for adhesion forces. The Johnson–Kendall–Roberts (JKR) model and the Derjaguin–Muller–Toporov (DMT) model describe extreme situations: the JKR model accounts for dominant adhesion forces in the contact zone, while the DMT model assumes dominant elastic resistance in the contact zone but non-negligible adhesion forces in the periphery of the contact zone. In the absence of any *a priori* knowledge on the relative strengths of the elastic and the adhesive contributions to the shape of the indentation curve,[24] we in the following consider both models.

The JKR model applies for soft materials with large surface energy and probes with a large curvature radius.[25] For a spherical indenter, the JKR model can be expressed by the following equations:[26]

$$\begin{aligned} \delta &= \frac{a_{JKR}{}^2}{R} - \frac{4}{3}\sqrt{\frac{a_{JKR}F_{ad}}{RK}} \\ a_{JKR} &= \left(\frac{R}{K}\right)^{1/3}\left(\sqrt{F_{ad}} + \sqrt{F_n + F_{ad}}\right)^{2/3} \\ F_{ad} &= \frac{3\pi}{2}\gamma R \end{aligned} \quad (2)$$

with the same notations as in eqn (1) and γ the interfacial energy and F_{ad} the adhesive pull-off force between the two surfaces. a_{JKR} denotes the contact radius that accounts for the deformation of the substrate that sticks to the probe. On the other hand, the DMT model applies for hard materials with low surface energy and probes with a small curvature radius.[25] For a spherical indenter, the DMT model can be written as[27]

$$\begin{aligned} F_n &= K\delta^{3/2}R^{1/2} - F_{ad} \\ F_{ad} &= 2\pi\gamma R \end{aligned} \quad (3)$$

with the same notations as above.

A characteristic parameter,[25,28]

$$\mu \sim (R\gamma^2/E^2)^{1/3}/z_0 \quad (4)$$

with z_0 being the equilibrium distance associated to the attractive potential, allows discriminating between JKR and DMT models. It measures the ratio between the normal elastic deformation caused by adhesion in the absence of applied load and the spatial range of the adhesion forces themselves. Thus large μ reveals strong adhesion in the short range and therefore supports the JKR model, while $\mu \ll 1$ reports that adhesion forces outside the contact region are not negligible and therefore promotes the DMT model. Consequently, to the zeroth order, the indenting force F_n is the interfacial force F_{ad} within the JKR assumptions. On the contrary, F_n opposes the elastic resistance within DMT assumptions, as the DMT model assumes that the deformation caused by the indentation is close to Hertz's prediction.[27] Replacing F_{ad} by F_n in Eqn (2) or neglecting F_{ad} in eqn (3) both lead to zeroth order to the scaling law:

$$F_n{}^{2/3} \sim \delta \quad (5)$$

The scaling law that relates the indentation force F_n to the indentation depth δ is to zeroth order identical to the case of the purely elastic, Hertz's model, although in the case of the JKR model, F_n is dominated by the adhesion force and not by the elastic resistance of the sample. Then, plotting the

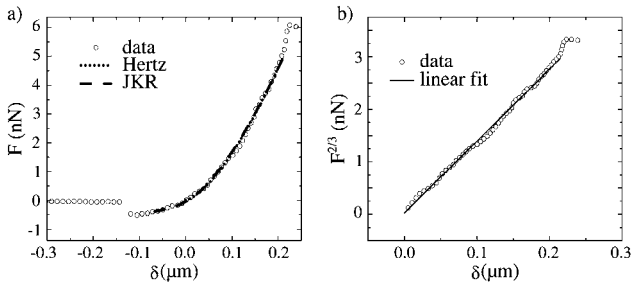

Fig. 1 (a) Experimental indentation curve $F(\delta)$ fitted by Hertz (dash dotted line) and JKR (dotted line) models. The DMT model superimposes the JKR model. The Hertz's model predicts a Young's modulus of 15.0 kPa and the DMT and JKR models predict 10.2 kPa. Fits were performed on the indentation range selected in (b). (b) A linear fit (–) of the experimental data (°) drawn as $F_n^{2/3}$ *vs.* indentation δ shows that experimental data deviate from the elastic models for indentation greater than 0.21 μm. This gives the upper limit for fitting the data.

indentation curve in the form of $F_n^{2/3}(\delta)$ allows marking out the boundaries of the validity of elastic or elasto-adhesive models (Fig. 1). Deviation of the curve from the straight line marks out the range of the indentation depths where the fitting model is appropriate. But it is worth noting that the consistency of the linearity between δ and $F_n^{2/3}$ for all the families of models does not allow evaluating the relevance of accounting for the surface energy. Adhesive forces can only be excluded after evaluating the relative weights of elastic and adhesive contributions obtained by the fit of the indentation curve. This differs from indentation curves obtained with a pyramidal indenter, where elasticity and adhesion contribute with distinct scaling laws.[29]

3 Results

This methodology was applied to the measurement of the Young's modulus of human pituitary gland tissues. Indentation measurements were performed on healthy parts of tumor resections (see Experimental section).

3.1 Measurement of the rigidity of pituitary tissue requires an elasto-adhesive model

Hertz, JKR and DMT models were used to fit the indentation curves. The results are illustrated in Fig. 2. The log-normal fits of these distributions are summarized in Table 1.

In order to evaluate the relevance of using an elasto-adhesive model compared to a Hertz's model, we quantified the differences between the fitting parameters that are predicted by all the models. In case an adhesive model would be unnecessary, fitting parameters should converge to Hertz's ones, with the interfacial energy $\gamma \to 0$. As shown in Fig. 2 and Table 1, this is not the case: fitting based on Hertz's model leads to a rigidity that is 90% larger than values obtained using elasto-adhesive models. Calculation of the characteristic length μz_0 (eqn (4)) shows that the description of the pituitary tissue gland stands in between JKR and DMT models: μz_0 is of the order of 1, which is of the order of the atomic distance z_0 that is expected for a Lennard Jones adhesive potential. Then models such as Maugis or Pietrement and Troyon[24] should be considered. However, as

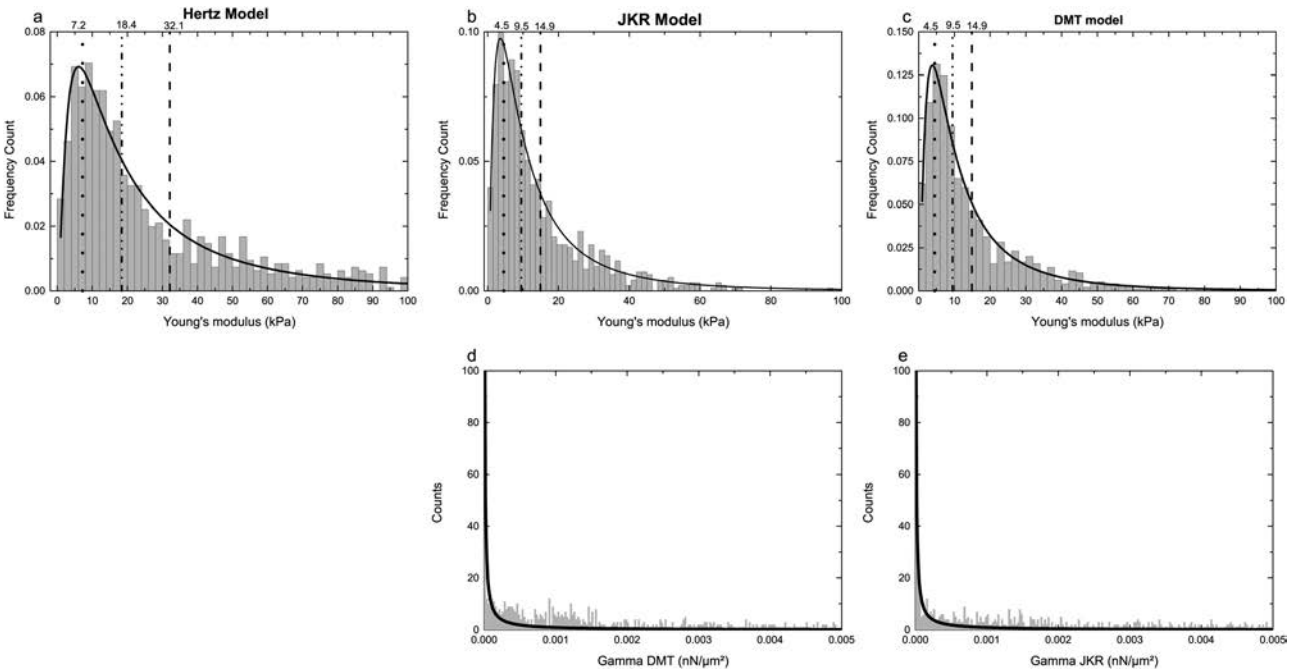

Fig. 2 Frequency counts of the Young's modulus E (a–c) and of the interfacial energy γ (d and e) of pituitary gland samples, using Hertz (a), JKR (b and d) and DMT (c and e) models to fit the indentation curves. Histograms are fitted using a log-normal distribution. In (a–c), the dotted line shows the peak of the distribution, the dash-dotted line marks the geometric mean, which is also the median, and the dashed line shows the arithmetic mean. Values are reported in Table 1.

Table 1 Young's moduli and interfacial energies obtained from the fits by Hertz, JKR and DMT models, and the intervals that account for 66% of the measurements

	Hertz	JKR	DMT
Geometric mean E (kPa)	18.4	9.5	9.5
Dispersion for E (kPa)	[6.2 55.8]	[3.5 25.9]	[3.5 25.8]
Geometric mean γ (kPa μm)	NA	2.3×10^{-5}	1.8×10^{-5}
Dispersion for γ (kPa μm)	NA	$[1.8 \times 10^{-9}$ 0.3]	$[1.6 \times 10^{-9}$ 0.2]
μz_0 (Å) (eqn (4))	NA	2.6	3.1
Mean E (kPa)	32.1	14.9	14.9
Standard deviation E (kPa)	43.4	15.7	15.7
Mean γ (kPa μm)	NA	4.6×10^{-3}	3.1×10^{-3}
Standard deviation γ (kPa μm)	NA	2.3×10^{-2}	1.5×10^{-2}
Mode E (kPa)	7.2	4.5	4.5
Mode γ (kPa μm)	NA	0	0

DMT and JKR models lead to values that are not significantly different, we keep for the sake of simplicity JKR and DMT fitting procedures.

3.2 Pituitary gland tissue bears elastic deformations up to a few nN

Fig. 1a shows that the pituitary tissue gland has an elastic response up to a few nN. This statistically representative indentation curve was fitted with a Young's modulus of 10.2 kPa and is elastic up to about 5 nN. Some curves representative of stiffer parts of the sample are elastic up to a higher load whereas for softer parts (lower than 1 kPa) the indentation is so huge (compared to the polystyrene bead indenter) that the curve deviates from the model below 1 nN due to indentation depth being more than the bead radius. Then by calculating the maximal stress imposed by the bead, we observed that pituitary gland tissue retains elasticity up to stresses in the range [0.2 1.2] kPa, with a geometric average of 0.5 kPa. This value is of similar order of magnitude as cell stresses of the order of kPa.[30,31] We can therefore conclude that cells in the pituitary gland tissue probe to some significant extent tissue elasticity. Considering the elastic regime of the rheological response of this tissue then makes sense from a physiological point of view.

3.3 Pituitary gland tissue is not viscous at μm s^{-1} speed of indentation

Many samples like polymers show strong dependency on the speed/frequency of the measurements.[23] This is also the case of brain tissues when macroscopically indented to depths that are larger than the limits of the elastic regime.[8] Here, we tested the influence of the indentation speed on the measured micron scaled Young's modulus, within the range of the dynamics of cellular forces. The amplitude of cellular tensions within cell adhesions is of order of nN, leading to μm scaled deformations within kPa materials.[30] Additionally, the propagation the cellular tensions in cells occurs within a few tens of seconds.[32,33] Then cell force-mediated deformations of the extracellular matrix are expected to occur with velocities of the order of μm s^{-1}. Fig. 3 shows the dependency of the measured stiffness of the pituitary gland tissue on the indentation speed in this range. It shows that

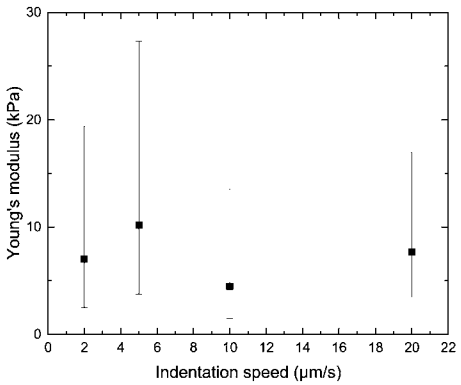

Fig. 3 Young's modulus obtained from the JKR model as a function of the indentation speed. Each point is the geometric average of at least 100 data points. Bars show the geometric dispersion.

values of the Young's modulus (and of the interfacial energy, data not shown) are independent of the indentation speed. We can therefore conclude that this tissue is not viscous in this range of velocity.

3.4 Pituitary gland tissue is 9.5 kPa in median

1285 indentation curves were recorded by force mapping on 9 maps of 95 × 95 μm^2 randomly distributed on 4.7 mm^2 within two pituitary gland tissue samples from one patient. The Young's modulus shows a geometric average of 9.5 kPa (Fig. 2 and Table 1). However, the dispersion of the Young's moduli is about 20 kPa, as shown in Table 1. Fig. 4a shows a representative map of such force mapping. It shows that within a 95 × 95 μm^2 window, the rigidity goes from less than 1 kPa to more than 50 kPa. This demonstrates that the pituitary gland tissue is highly heterogeneous at the cell scale.

3.5 Pituitary gland tissue bears kPa μm^{-1} gradients of rigidity

Fig. 4b shows a representative map of the gradient of the stiffness within pituitary gland tissue. Local changes in stiffness were measured up to 12 kPa μm^{-1}. In this tissue, the geometric mean of the gradients is 2.2 kPa μm^{-1}. Thus pituitary gland tissue bears kPa μm^{-1} gradients of rigidity at micron scales, *i.e.* at scales that

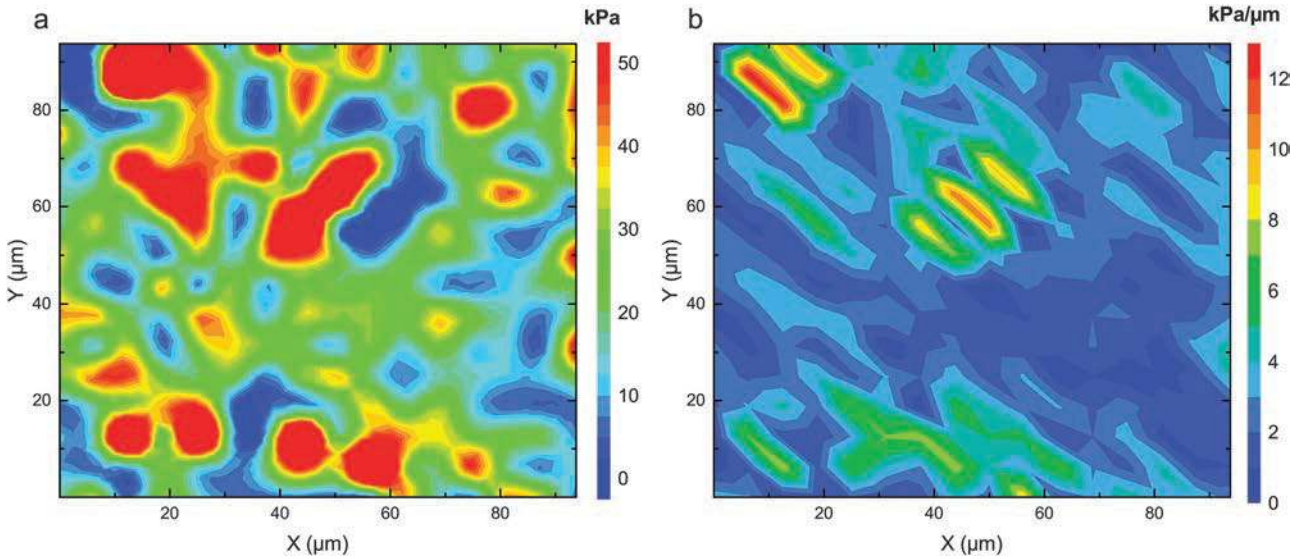

Fig. 4 (a) Young's modulus map of a pituitary gland tissue showing that local elastic properties of this gland are heterogeneous. (b) Map of the spatial gradient of the Young's modulus shows values up to 12 kPa μm^{-1}.

are large compared to the molecular structure of the extracellular matrix but smaller than cell size.

4 Discussion

Measuring the Young's modulus of brain tissues is a crucial challenge for neurological studies. For diagnosis, it could help in assessing tumors[34] whereas for fundamental research it could help in understanding neurodegenerative diseases and probably the action mechanisms of tumor spreading.[35] It is also a critical input for modeling traumatic brain injuries, where brain stiffness has a dramatic influence on tissue reparation.[36] The mechanical properties of brain tissues have been explored for many years (see ref. 37 for a review), and macroscopic *in vitro* and *in vivo* measurements have revealed that brain tissues respond visco-elastically to strains up to 30%. The pituitary gland escaped these extensive studies probably because its sub-centimeter size prevents the use of non-intrusive techniques such as MRE. However, hormone secretions from this gland are critical to the control of basic functions such as temperature regulation or blood pressure, and pituitary tumors are quite widespread. Then adding the mechanical characteristics of this organ to the database of brain tissues makes sense. Here we propose the first quantification of the elastic properties of pituitary gland tissues.

We found that the human pituitary gland tissue of this patient responded elastically to micron scaled indentations with velocities below 20 μm s^{-1}. The measured rigidity was 9.5 kPa in median, with 66% of the values falling in the interval [3.5 25.9] kPa. These results are to be compared to the visco-elastic properties of the white and grey matters of dead pigs or live humans obtained by IT-AFM,[38] macroscopic indentation,[39,40] or elastography.[41] Depending on the methods, the storage moduli vary from 0.3 to about 2 kPa, while the loss moduli are of similar amplitude. The pituitary gland is expected to be stiffer, as experienced by surgeons. Our result then fits with this intuition. The rigidity distribution we find should however be complemented with tissues from other patients to improve its statistical relevance. Nevertheless, the preparation protocol is not expected to influence this value as we could check that tissue integrity was not altered by the freezing process (reticulin staining,[42] data not shown). Our finding that the tissue is not viscous differs from the state-of-the-art, and is to be reported to the speeds of indentation we probe. For instance, our result does not give information in the context of much more rapid impacts such as in traumatic brain injury.[40]

The goal of this work is to offer not only a macroscopic, statistical description of the rigidity of this organ as discussed previously, but also the characterization of the micron scaled variations of the rigidity. Nowadays, adenomas in the pituitary gland are localized by MRI, as long as they can fix contrast agents. Otherwise, the surgeon has to perform exploratory surgery and occasionally removes healthy tissues, similar to the samples that we used in this study. Getting an additional *in vivo* marker for tumor tissues in the pituitary gland could help limiting the removal of healthy tissues. Rigidity and gradients of rigidity could be such markers. Other studies have already shown in breast,[43] lung[44] or liver[45] tissues that tumor tissues have different mechanical properties. Concerning pituitary gland tissues, the gradient of rigidity could also be informative on the state of progress of the cancer as these tumors are characterized by degradation of the extracellular matrix.[42] Then, the statistical descriptors of the distribution of rigidity values and of the gradients of rigidity that are met in this organ would serve as a reference.

Micron-scaled variations of rigidity are also of interest in a different context. They could influence cell adhesion and migration, as cell mechanosensitivity is suspected to occur at least partly at the scale of the cellular adhesions, of a few μm^2.[15,16,46] Then mapping rigidity variations in organs could become very informative in the context of understanding the mechanisms at the origin of tumor spreading.[47]

In order to probe the rigidity of the pituitary gland tissue averaged on micron scaled areas, we performed AFM-controlled indentation with a spherical indenter of 10 μm diameter. This allows mapping the tissue at the subcellular scale but still at a large scale compared to the matrix mesh. Compared to nano-scaled indentation performed with pyramidal tips, using an indenter with a large surface of contact brings the additional contribution of an attractive interaction between the tip and the sample. This contribution scales similarly to linear elasticity, and therefore must be explicitly accounted in the models that are used to quantify the elastic response from the indentation curve.

As mentioned in Section 2, the choice of the part of the indentation curve that is used to extract the fitting parameters, namely the Young's modulus, the interfacial energy and the position of the contact point, is critical and strongly influences the result. In the present work, we account for the interfacial energy that influences the indentation curve close to the contact point. Then the remaining pitfall is to fit the curve out of the elastic regime. For this purpose, we set up a criterion to select the region of the curve that corresponds to the linear elastic response. We demonstrated that in the presence of an interfacial energy, the indentation force F_n scales to zeroth order with the indentation depth δ as $F_n \propto \delta^{3/2}$, as it is the case in the absence of adhesion. It is however to be noted that F_n is the elastic resistance of the sample only when adhesion comes to second order as in the DMT model. F_n is predominantly the adhesion force in the case of a strong adhesive interaction between the probe and the sample as in the JKR model. Then when replotting the indentation curve $F_n(\delta)$ in the form ${F_n}^{2/3}(\delta)$, the elasto-adhesive regimes appear as straight lines (Fig. 1). This one step approach thus offers a fast method for determining the range of the indentation curve for which the models are appropriate. Compared to the well established sliding window method,[21,22] this methodology is much faster and also allows tackling multi-layered samples (see ESI†).

Here, we showed that the adhesive interaction between the probe and the tissue cannot be neglected. Hertz's model, which only accounts for the elastic resistance of the tissue to indentation, overestimates the Young's modulus of more than 90% (Table 1). The fact that we find a larger Young's modulus when neglecting adhesion is surprising as one would expect that an adhesive interaction would suck the probe and therefore increase the deflection of the tip compared to a non-adhesive sample. The reason is that, in principle, all the models would predict the same Young's modulus if the sample would bear elastic deformation up to infinite forces. The difference between Hertz's and adhesive models comes from the fact that the fit can only be performed on a limited indentation range where the sample retains its elastic nature (see Fig. 1b). In this range, Hertz's fit is strongly influenced by the shape of the curve in the vicinity of the contact point for which it is not relevant in the presence of adhesion. Adhesive models are built to describe this region and are therefore less sensitive to the finite range of the indentation curve.

Following previous work,[24] we explored the relevance of the elasto-adhesive model that we used to fit the indentation curve. We found that the adhesive interaction between the probe and the sample occurs at the atomic length scale (eqn (4)). Then the DMT and JKR models we used are in principle not appropriate, and Maugis or Pietrement and Troyon models should be considered.[24] As both DMT and JKR lead to non-significantly different values (Table 1), different outcomes are not expected with refining of the description of the adhesive interaction. We therefore kept DMT and JKR models to set up the fitting methodology of the indentation curve.

Using this methodology, our major result is that the rigidity of the pituitary gland tissue is very heterogeneous at the micron scale. Gradients up to 12 kPa μm^{-1} were observed (Fig. 4). This result is expected when performing a mechanical mapping with a nanoscaled probe, such as a pyramidal tip. Then it measures the spatial heterogeneities at the molecular level of the texture of the extracellular matrix for instance. Indeed, ref. 43 used this approach to show that cancer tissues from breast biopsies are more loose than healthy tissues. Our observation shows that mechanical heterogeneities with a similar amplitude of kPa μm^{-1} also exist at larger scale. Here these may be micron scaled self-assemblies of macromolecules such as collagen IV bundles or collagen/elastin/laminin/fibronectin/reticulin fibrous scaffolds,[48] together with cells that are probed. Macromolecules organized as dense fibers could then lead to rigidity of several tens of kPa,[49] while cells or macromolecules in gel-like structures would give rise to rigidity values of the order of kPa or below.[50]

This observation is of importance as it shows that *in vivo*, cells meet gradients of rigidity that are at subcellular scales. And indeed, previous studies have already emphasized the contribution of gradients of rigidity in the development of the central nervous system[36] and in stem cell differentiation,[51] but in both cases, their main focus was millimeter scaled rigidity gradients. Regarding the already emphasized contribution of micron scaled rigidity in cell adhesion and migration,[15,16] it then suggests that subcellular gradients of rigidity should also be accounted for in *in vitro* experiments, as they correspond to physiological conditions.

5 Conclusion

Mechanical indentation using AFM on sliced human pituitary gland tissues revealed that the mechanical properties of this tissue are highly heterogeneous, with 66% of the values dispersed between 3.5 and 25.9 kPa, and with a geometric mean of 9.5 kPa. This dispersion is accompanied by kPa μm^{-1} gradients of rigidity at the micron scale. Only smoother, kPa mm^{-1}, gradients have presently been explored, and have been shown to orient cell movement.[36,51,52] The impact of such strong, subcellular gradients on cell behavior is now to be elucidated, as molecular autonomous rigidity sensors have already been identified within cell focal adhesions.[13,15]

6 Experimental section

6.1 Tissue preparation

Pituitary tissue samples were obtained from the University Hospital Grenoble, Department of Neurosurgery. Informed written consent

was obtained from the patients or their families. Pituitary tissue samples were collected from the operating room during transphenoidal surgery and were immediately frozen at −80 °C. Frozen tissues, whose sizes were below 1 mm^2, were cut (150 μm in thickness) from the surgical specimen using a cryostat and tissue slices were deposited on glass slides and stored at −20 °C. Then the tissue slices was stained for reticulin, a protein of the extracellular matrix of the pituitary gland. The organization of this protein in a regular mesh is a marker of the integrity of the tissue and allows discriminating between healthy and tumor tissues.[42] Slices from samples with a fully intact reticulin scaffold were used for this study. Before proceeding to IT-AFM, the tissue slice was incubated at 26 °C for 30 minutes and then encircled with a hydrophobic fat pen (Dako pen) to create an incubation space. A washing was carried out with filtered PBS in order to remove residues of the hydrophobic barrier. The sample was then immediately immersed in filtered PBS and AFM measurements were performed within the next 1–2 h at room temperature.

6.2 AFM measurements

Young's moduli of brain tissue samples are measured on a Nanowizard II AFM (JPK Instruments, Berlin) in the force mapping mode. MLCT D tipless cantilevers (Bruker, Santa Barbara) with a nominal spring constant of 0.03 N m^{-1} are chosen for their ability to address Young moduli between 0.1 and 100 kPa. A 10 μm polystyrene sphere was glued to the cantilever in order to average the elastic properties on a micron-sized area, *i.e.* averaging on both cells and extracellular matrix material properties. The Poisson's ratio used for this experiment is 0.45.[53]

For all experiments, indentation speed is set from 1 to 20 μm s^{-1} allowing us to check if the sample has any viscoelastic properties in this range. Practically, we probed different locations of a specific tissue slice with distinct speeds and obtained statistically representative values of the rigidity for each indenting velocity. We ensured an indentation depth below 3 μm by adjusting the nominal force set-point within 1 to 6 nN depending on the sample stiffness. The maps have a size of 95 × 95 μm^2 and represent at least 100 force curves. Force-indentation curves are then fitted with the models described below in the range of indentation specified by the criterion presented in Section 2.

6.3 Data post-treatment

Retract indentation curves were plotted as described in Section 2, in the form $F^{2/3}(\delta)$. The *de visu* straight portion of the curve was fitted by a straight line (Fig. 1). Deviation of the curve from the straight line marks out the boundaries of the indentation depth on which the fitting model is relevant. The Young's modulus E and the interfacial energy γ were then obtained by fitting the curve in this range by Hertz (eqn (1)), JKR (eqn (2)) and DMT (eqn (3)) models.

The determination of the contact point is also crucial in data post-treatment.[21,24] In our case, the contact point is a fit parameter in eqn (1)–(3). We replaced δ in eqn (1)–(3) by $\delta - \delta_0$, with δ the indentation that is calculated using the AFM software assuming that the zero is at the crossing of the indentation curve with $F_n = 0$, and δ_0 the true position of the zero relative to this choice. Guess of this fit parameter is chosen at the minimum of the attractive well of the indentation curve for the JKR and DMT models, and at the indentation that corresponds to $F_n = 0$ for the Hertz model (then $\delta_0 = 0$).

6.4 Statistical analysis

Young's modulus and interfacial energy are obtained by analyzing the distribution of 1285 indentation curves taken on two pituitary gland tissue samples from one patient. As a whole, the AFM scan is performed on 9 maps of 95 × 95 μm^2 randomly distributed on 4.7 mm^2. For all models, the fitting parameters are log-normally distributed. We therefore present the results using the geometric mean $\langle x \rangle_G$ and the geometric standard deviation σ_G to account for the 2/3 of the values that stand in between $\langle x \rangle_G/\sigma_G$ and $\langle x \rangle_G \cdot \sigma_G$.[54] The literature usually uses the arithmetic mean and standard deviation to give a representative value of the Young's moduli. We therefore also mention them for comparison.

Acknowledgements

N. B. and A. N. acknowledge the support by ANR-12-JSVE05-0008. The authors are indebted to the AFM platform of the Interdisciplinary Laboratory of Physics, Grenoble, France, for their hosting.

References

1 I. Levental, P. C. Georges and P. A. Janmey, *Soft Matter*, 2007, **3**, 299–306.
2 L. Z. Shuck and S. H. Advani, *J. Basic Eng.*, 1972, **94**, 905–911.
3 M. Hrapko, J. van Dommelen, G. Peters and J. Wismans, *Biorheology*, 2006, **43**, 623–636.
4 M. Z. Kiss, T. Varghese and T. J. Hall, *Phys. Med. Biol.*, 2004, **49**, 4207–4218.
5 H. H. Bayraktar, E. F. Morgan, G. L. Niebur, G. E. Morris, E. K. Wong and T. M. Keaveny, *J. Biomech. Eng.*, 2004, **37**, 27–35.
6 Y. K. Mariappan, K. J. Glaser and R. L. Ehman, *Clin Anat*, 2010, **23**, 497–511.
7 J.-L. Gennisson, T. Deffieux, M. Fink and M. Tanter, *Diagn Interv Imaging*, 2013, **94**, 487–495.
8 T. P. Prevost, G. Jin, M. A. de Moya, H. B. Alam, S. Suresh and S. Socrate, *Acta Biomater.*, 2011, **7**, 4090–4101.
9 T. Lyyra, I. Kiviranta, U. Väätäinen, H. J. Helminen and J. S. Jurvelin, *J. Biomed. Mater. Res.*, 1999, **48**, 482–487.
10 D. E. Discher, P. Janmey and Y.-L. Wang, *Science*, 2005, **310**, 1139–1143.
11 C. Yang, M. W. Tibbitt, L. Basta and K. S. Anseth, *Nat. Mater.*, 2014, **13**, 645–652.
12 K. M. Yamada and E. Cukierman, *Cell*, 2007, **130**, 601–610.
13 S. Ghassemi, G. Meacci, S. Liu, A. A. Gondarenko, A. Mathur, P. Roca-Cusachs, M. P. Sheetz and J. Hone, *Proc. Natl. Acad. Sci. U. S. A.*, 2012, **109**, 5328–5333.
14 A. Pasapera, S. Plotnikov, R. Fischer, L. Case, T. Egelhoff and C. Waterman, *Curr. Biol.*, 2015, **25**, 175–186.
15 S. V. Plotnikov, A. M. Pasapera, B. Sabass and C. M. Waterman, *Cell*, 2012, **151**, 1513–1527.

16 H. Wolfenson, G. Meacci, S. Liu, M. R. Stachowiak, T. Iskratsch, S. Ghassemi, P. Roca-Cusachs, B. O'Shaughnessy, J. Hone and M. P. Sheetz, *Nat. Cell Biol.*, 2016, **18**, 33–42.
17 K. Franze, *Development*, 2013, **140**, 3069–3077.
18 A. Gefen and S. S. Margulies, *J. Biomech. Eng.*, 2004, **37**, 1339–1352.
19 M. Destrade, M. Gilchrist, J. Murphy, B. Rashid and G. Saccomandi, *Int J Non Linear Mech*, 2015, **75**, 54–58.
20 D. C. Lin, E. K. Dimitriadis and F. Horkay, *J. Biomech. Eng.*, 2007, **129**, 430–440.
21 J. Domke and M. Radmacher, *Langmuir*, 1998, **14**, 3320–3325.
22 E. K. Dimitriadis, F. Horkay, J. Maresca, B. Kachar and R. S. Chadwick, *Biophys. J.*, 2002, **82**, 2798–2810.
23 B. Cappella, S. K. Kaliappan and H. Sturm, *Macromolecules*, 2005, **38**, 1874–1881.
24 D. C. Lin, E. K. Dimitriadis and F. Horkay, *J. Biomech. Eng.*, 2007, **129**, 904–912.
25 D. Maugis, *J. Colloid Interface Sci.*, 1992, **150**, 243–269.
26 K. L. Johnson, K. Kendall and A. D. Roberts, *Proc. R. Soc. London, Ser. A*, 1971, **324**, 301–313.
27 B. Derjaguin, V. Muller and Y. Toporov, *J. Colloid Interface Sci.*, 1975, **53**, 314–326.
28 D. Tabor, *J. Colloid Interface Sci.*, 1977, **58**, 2–13.
29 L. Sirghi, J. Ponti, F. Broggi and F. Rossi, *Eur. Biophys. J.*, 2008, **37**, 935–945.
30 U. Schwarz, *Soft Matter*, 2007, **3**, 263–266.
31 V. Maruthamuthu, B. Sabass, U. S. Schwarz and M. L. Gardel, *Proc. Natl. Acad. Sci. U. S. A.*, 2011, **108**, 4708–4713.
32 C. Grashoff, B. D. Hoffman, M. D. Brenner, R. Zhou, M. Parsons, M. T. Yang, M. A. McLean, S. G. Sligar, C. S. Chen, T. Ha and M. A. Schwartz, *Nature*, 2010, **466**, 263–266.
33 P. Heil and J. P. Spatz, *J. Phys.: Condens. Matter*, 2010, **22**, 194108.
34 Y. Jamin, J. K. Boult, J. Li, S. Popov, P. Garteiser, J. L. Ulloa, C. Cummings, G. Box, S. A. Eccles, C. Jones, J. C. Waterton, J. C. Bamber, R. Sinkus and S. P. Robinson, *Cancer Res.*, 2015, **75**, 1216–1224.
35 T. A. Ulrich, E. M. de Juan Pardo and S. Kumar, *Cancer Res.*, 2009, **69**, 4167–4174.
36 K. Franze, P. A. Janmey and J. Guck, *Annu. Rev. Biomed. Eng.*, 2013, **15**, 227–251.
37 S. Chatelin, A. Constantinesco and R. Willinger, *Biorheology*, 2010, **47**, 255–276.
38 A. F. Christ, K. Franze, H. Gautier, P. Moshayedi, J. Fawcett, R. J. M. Franklin, R. T. Karadottir and J. Guck, *J. Biomech.*, 2010, **43**, 2986–2992.
39 S. Budday, R. Nay, R. de Rooij, P. Steinmann, T. Wyrobek, T. C. Ovaert and E. Kuhl, *J. Mech. Behav. Biomed. Mater.*, 2015, **46**, 318–330.
40 B. Rashid, M. Destrade and M. D. Gilchrist, *J. Mech. Behav. Biomed. Mater.*, 2012, **10**, 23–38.
41 C. L. Johnson, J. L. Holtrop, M. D. McGarry, J. B. Weaver, K. D. Paulsen, J. G. Georgiadis and B. P. Sutton, *Magn. Reson. Med.*, 2014, **71**, 477–485.
42 S. Noh, S. H. Kim, N. H. Cho and S. H. Kim, *Endocr. Pathol.*, 2015, **26**, 178–184.
43 M. Plodinec, M. Loparic, C. A. Monnier, E. C. Obermann, R. Zanetti-Dallenbach, P. Oertle, J. T. Hyotyla, U. Aebi, M. Bentires-Alj, R. Y. H. Lim and C.-A. Schoenenberger, *Nat. Nanotechnol.*, 2012, **7**, 757–765.
44 F. Liu and D. J. Tschumperlin, *J. Visualized Exp.*, 2011, **54**, 2911.
45 M. Tian, Y. Li, W. Liu, L. Jin, X. Jiang, X. Wang, Z. Ding, Y. Peng, J. Zhou, J. Fan, Y. Cao, W. Wang and Y. Shi, *Nanoscale*, 2015, **7**, 12998–13010.
46 S. Ghassemi, N. Biais, K. Maniura, S. J. Wind, M. P. Sheetz and J. Hone, *J. Vac. Sci. Technol., B: Microelectron. Nanometer Struct. – Process., Meas., Phenom.*, 2008, **26**, 2549–2553.
47 M. J. Paszek, N. Zahir, K. R. Johnson, J. N. Lakins, G. I. Rozenberg, A. Gefen, C. A. Reinhart-King, S. S. Margulies, M. Dembo, D. Boettiger, D. A. Hammer and V. M. Weaver, *Cancer Cell*, 2005, **8**, 241–254.
48 J. J. Evans and K. Chitcholtan, *Open Neuroendocrinol. J.*, 2011, **4**, 111–119.
49 J. Silverberg, A. Barrett, M. Das, P. Petersen, L. Bonassar and I. Cohen, *Biophys. J.*, 2014, **107**, 1721–1730.
50 S. E. Cross, Y.-S. Jin, J. Tondre, R. Wong, J. Rao and J. K. Gimzewski, *Nanotechnology*, 2008, **19**, 384003.
51 J. R. Tse and A. J. Engler, *PLoS One*, 2011, **6**, e15978.
52 B. C. Isenberg, P. A. Dimilla, M. Walker, S. Kim and J. Y. Wong, *Biophys. J.*, 2009, **97**, 1313–1322.
53 G. Soza, R. Grosso, C. Nimsky, P. Hastreiter, R. Fahlbusch and G. Greiner, *Int J Med Robot*, 2005, **1**, 87–95.
54 E. Limpert and W. A. Stahel, *PLoS One*, 2011, **6**, e21403.